Published in final edited form as:
IEEE Trans Image Process. 2011 January ; 20(1): 176–185. doi:10.1109/TIP.2010.2059033.

Tomographic Reconstruction of Gated Data Acquisition Using DFT Basis Functions

Xiaofeng Niu [Student Member, IEEE] and **Yongyi Yang [Senior Member, IEEE]**
Department of Electrical and Computer Engineering, Illinois Institute of Technology, Chicago, IL 60616, USA

Abstract

In image reconstruction gated acquisition is often used in order to deal with blur caused by organ motion in the resulting images. However, this is achieved almost inevitably at the expense of reduced signal-to-noise ratio in the acquired data. In this work, we propose a reconstruction procedure for gated images based upon use of discrete Fourier transform (DFT) basis functions, wherein the temporal activity at each spatial location is regulated by a Fourier representation. The gated images are then reconstructed through determination of the coefficients of the Fourier representation. We demonstrate this approach in the context of single photon emission computed tomography (SPECT) for cardiac imaging, which is often hampered by the increased noise due to gating and other degrading factors. We explore two different reconstruction algorithms, one is a penalized least-square approach and the other is a maximum *a posteriori* approach. In our experiments, we conducted a quantitative evaluation of the proposed approach using Monte Carlo simulated SPECT imaging. The results demonstrate that use of DFT-basis functions in gated imaging can improve the accuracy of the reconstruction. As a preliminary demonstration, we also tested this approach on a set of clinical acquisition.

Index Terms

Cardiac single photon emission computed tomography (SPECT); discrete Fourier transform (DFT); gated reconstruction; spatiotemporal reconstruction

I. Introduction

In this work we propose a joint estimation approach for reconstruction of images from a gated data acquisition. In a gated study, the imaging period is divided into a number of smaller time intervals, the purpose being to reduce motion blur in the resulting images. The gating can be either cardiac or respiratory or both. For example, in gated cardiac imaging, the cardiac cycle is divided into a number of smaller intervals (typically between eight and 16) based upon the recorded electrocardiogram (ECG) signal, and the image is reconstructed for each interval. This not only alleviates the blur caused by cardiac motion, but also can provide valuable information about the ventricular function, including wall motion, ejection fraction and left ventricle volume [1]. However, due to reduced data counts (or shortened exposure time) within individual gate intervals, the resulting images often suffer from increased noise.

In recent years, there have been significant interests in development of spatiotemporal methods to combat the increased noise associated with gated imaging. To name a few, in [2] multislice CT scans are simultaneously collected with digital spirometry to correct for breathing motion; in [3], a reconstruction procedure based upon respiratory motion correction was proposed using PET list mode data; in [4], heart motion was imaged using isolated spectral peaks in SPAMM-tagged MR images; in [5], a nonrigid image summing method was proposed via optical flow over different gates in gated PET; in [6] a Fourier filtering OSEM with a binomial model was applied in gated single photon emission computed tomography (SPECT); in our previous work [7], spatiotemporal reconstruction methods based upon motion compensation were developed to reduce noise and motion blur in gated SPECT.

A common theme among these spatiotemporal methods is to exploit the statistical correlation among the different gate frames in a sequence in which the observed noise is typically uncorrelated along the gate dimension. For example, the different gate frames in a cardiac sequence would be identical if it were not for the cardiac motion. Thus, it would be most effective to enforce smoothing along the motion trajectories in the gate frames during reconstruction. A challenge in such an approach, however, is that the relative motion between the different gates is not known *a priori*; consequently, it has to be estimated from the noisy data either by applying motion estimation or image registration which could be challenging by itself.

In this work, we explore an alternative approach for spatiotemporal reconstruction, which can obviate the explicit need for motion estimation. Instead of relying on a prior that is explicitly based upon image motion, we model at each spatial location the image intensity across the different gates by a set of Fourier harmonic basis functions. This is motivated by the fact that the image function is essentially periodic over the gating intervals owning to the periodic nature of underlying motion. In the resulting image representation, the image motion is modeled implicitly by the temporal variation in image intensity at a given spatial location. For example, consider the case of a gated cardiac sequence. The image intensity at a spatial location that experiences wall motion will vary across the different gates in a periodic fashion during the cardiac cycle, which can be modeled efficiently by a Fourier harmonic function of the gate intervals.

With a Fourier representation model, reconstruction of the different gate frames is obtained in a collective fashion by estimating the model coefficients. This can be potentially beneficial in that it can take advantage of the statistics of all the acquired data. Moreover, by varying the number of high-order basis functions used in the representation model, one can directly incorporate a temporal smoothing scheme that is spatially adaptive into the reconstruction procedure. For example, in regions that experience more motion higher order harmonic components can be used than in a background region with little or no motion.

For reconstruction, we develop two different methods for estimating the model coefficients: one is based upon penalized least-squares (PLS) estimation, and the other is based upon maximum *a posteriori* (MAP) estimation. In the PLS method, the model coefficients are estimated independently for the different Fourier harmonics, whereas in the MAP method they are determined in a simultaneous fashion by taking into account the noise statistics of the acquired data. While in theory being suboptimal, the PLS method can be favorable in terms of its computational complexity. This is particularly true when the gated sequence can be represented well with only a few lower order harmonic components. In such a case, one may simply discard higher order components without significantly sacrificing the reconstruction quality, leading to faster reconstruction.

To facilitate development in the rest of the paper we will present our methods in the context of cardiac imaging using single-photon emission computed tomography (SPECT), which is currently the most frequently performed study in clinical nuclear medicine. However, it is noted that the proposed approach should be equally applicable to other imaging modalities as well, including positron emission tomography (PET), CT, or MRI, where the gating can be either cardiac or respiratory.

The concept of the proposed approach was first developed in our previous work [8], [9], where it was demonstrated with preliminary results using 2-D image slices. In this work, we further develop and demonstrate this approach by extending it to fully 3-D volumetric reconstruction, where two important degradation factors, namely attenuation and scatter, are also included in the reconstruction process. In our experiments, the proposed approach was first demonstrated using Monte Carlo simulated SPECT imaging. The use of simulated images allowed us to quantitatively evaluate the reconstructed images where the ground truth was known. As a preliminary demonstration, we also tested our approach on a set of clinical acquisition.

The rest of the paper is organized as follows: the imaging model, Fourier harmonic representation, and reconstruction methods are described in Section II. Evaluation methods are presented in Section III. The results and discussions are given in Section IV. Conclusions are given in Section V.

II. Reconstruction of Gated Image Sequence

A. Imaging Model

In gated imaging, the acquired projection data are binned into K gate intervals. The imaging data are described by the following model:

$$E[\mathbf{g}_k]=\mathbf{H}\mathbf{f}_k+\mathbf{r}_k,\ k=1,2,\ldots,K \quad (1)$$

where $\mathbf{g}_k$, $\mathbf{f}_k$, and $\mathbf{r}_k$ are vectors representing the acquired data (sinogram), original image, and expected scatter component, respectively, in gate k, $\mathbf{H}$ is the system matrix describing the imaging process in which each element h_{ij} represents the probability that a photon emitted at voxel location j is detected at detector bin i without being scattered, and $E[\cdot]$ is the expectation operator.

In this study, the system matrix $\mathbf{H}$ is modeled after SPECT imaging, of which the elements h_{ij} include both the distance-dependent point spread function (PSF) and the attenuation effect.

Our goal is to estimate the images $\mathbf{f}_k$ given the sinogram data $\mathbf{g}_k$, k= 1, 2, … K. Due to the low count level in the data and ill-conditioned nature of the system matrix $\mathbf{H}$, a direct inversion of the imaging equation in (1) would lead to very noisy images. Instead, we explore a joint reconstruction approach in which the different gate frames are reconstructed in a collective fashion. The goal is to exploit the fact that the different gate frames are essentially similar to each other except for the motion. Specifically, we will make use of a discrete Fourier transform (DFT) basis representation to regulate the time activities at each spatial location across the different gates, which are periodic owing to the periodic motion.

B. DFT Basis Function Model

We model the image activity at voxel j over different gate intervals by using a Fourier series as following:

$$f_k(j)=\sum_{m=0}^{K-1} d_m(j)e_m(k),\ j=1,\ldots,N,\quad k=1,\ldots,K \quad (2)$$

where $f_k(j)$ represents the image intensity at voxel j in gate interval k, $e_m(k)$ denotes the mth DFT basis function in the form $e_m(k)=(1)/(\sqrt{K})\exp(\sqrt{-1}\cdot 2\pi m(k-1)/K)$, $d_m(j)$denotes its corresponding coefficient, and Ndenotes the number of voxels in a gate frame.

Substituting the representation in (2) into the imaging model in (1), we obtain

$$E[\mathbf{g}_k]=\sum_{m=0}^{K-1} e_m(k)\mathbf{H}\mathbf{d}_m+\mathbf{r}_k,\ k=1,2,\ldots,K \quad (3)$$

where $\mathbf{d}_m$ is a vector representing the collection of the mth frequency coefficients $d_m(j)$ over all voxels.

Equation (3) directly relates the projection data to the frequency domain representation of the gated frames. Our goal is to estimate the unknown coefficients $\mathbf{d}_m$ associated with the different DFT basis functions.

As can be seen, by varying the number of high-order harmonics (i.e., high frequency components) in the representation in (2), we can achieve different degrees of smoothing along the gate dimension. Thus, such a DFT basis representation model offers the flexibility that one can directly incorporate a temporal smoothing scheme (i.e., across the gates) into the reconstruction procedure in a spatially adaptive manner. For example, the AC coefficients can be treated as zero at background voxels that are not associated with any motion. This will lead to fewer unknowns to estimate, and consequently, faster reconstruction algorithms.

Next, we describe two methods for estimating the unknown coefficients $\mathbf{d}_m$. The first method is based upon a PLS approach, in which the unknown coefficients are estimated separately for the different basis functions. The second method is based upon MAP estimation, in which the unknown coefficients are estimated in a collective fashion.

C. PLS Estimate

Due to the unitary property of the harmonic basis functions, we can obtain from (3) the following:

$$E\left[\sum_{k=1}^{K}\bar{e}_m(k)\mathbf{g}_k\right]=\mathbf{H}\mathbf{d}_m+\sum_{k=1}^{K}\bar{e}_m(k)\mathbf{r}_k \quad (4)$$
$$m=0,\ldots,K-1$$

where $\bar{e}_m(k)$ denotes the complex conjugate of $e_m(k)$.

Let $\mathcal{G}_m=\sum_{k=1}^{K}\bar{e}_m(k)\mathbf{g}_k$, which is noted to be the DFT of the projection data taken along the gate dimension; similarly, let $\mathbf{R}_m=\sum_{k=1}^{K}\bar{e}_m(k)\mathbf{r}_k$. Then, the above can be rewritten as

$$E[\mathcal{G}_m]=\mathbf{H}\mathbf{d}_m+\mathbf{R}_m, m=0,\ldots,K-1. \quad (5)$$

From (5) it can be seen that the unknown coefficients $\mathbf{d}_m$ are now decoupled from each other for the different basis functions. Thus, they can be estimated in a separate fashion. A note is that when the activity function in (2) is real-valued, the coefficients $\mathbf{d}_m$ are conjugate symmetric, i.e., $\mathbf{d}_m = \bar{\mathbf{d}}_{K-m}$. In such a case, we need to estimate about only one half of the unknown coefficients.

Observe that (5) bears the same form as the imaging model in (1). Therefore, it can be solved in the same fashion as in standard image reconstruction.

Specifically, note that the data term $\mathcal{G}_m$ is formed by a weighted average of K independent measurements. We can approximate its noise statistics by a Gaussian distribution model, and apply a least-squares approach to estimate $\mathbf{d}_m$. To compensate for the ill-conditioned nature of the system matrix $\mathbf{H}$, we introduce a Gibbs prior to impose spatial smoothing on $\mathbf{d}_m$. This leads to the following penalized quadratic objective function:

$$\mathbf{J}(\mathbf{d}_m)=\|\mathbf{H}\mathbf{d}_m+\mathbf{R}_m-\mathcal{G}_m\|^2+\beta_s\|\mathbf{Q}\mathbf{d}_m\|^2 \quad (6)$$

where $\mathbf{Q}$ is a spatial operator used to enforce local smoothness, and β_s is a scalar parameter used to control the degree of spatial smoothing.

The unknown $\mathbf{d}_m$ is estimated as

$$\widehat{\mathbf{d}}_m=\arg\min_{\mathbf{d}_m}\{\mathbf{J}(\mathbf{d}_m)\}, m=0,\ldots,K-1. \quad (7)$$

In our experiments, the first-order difference operator was used for $\mathbf{Q}$. Specifically, the penalty term $\|\mathbf{Q}\mathbf{d}_m\|^2$ is given by

$$\|\mathbf{Q}\mathbf{d}_m\|^2=\sum_{j=1}^{N}\sum_{i\in\aleph_j}|d_m(j)-d_m(i)|^2 \quad (8)$$

where $\aleph_j$ denotes a 26-voxel neighborhood around voxel j. As can be seen, this quantity is used to impose a penalty when the signal at a voxel is significantly different from that of its immediate neighbors.

Note that both operators $\mathbf{H}$ and $\mathbf{Q}$ are real-valued. Thus, the real and imaginary parts of $\mathbf{d}_m$ can be solved separately from their respective counterparts of $\mathbf{R}_m$ and $\mathcal{G}_m$. It is noted that the optimization in (7) is of the form of a standard PLS problem. In our experiments, a preconditioned gradient descent algorithm was used, where a diagonal positive-definite preconditioner was used to adjust the gradient as in [10], [11]. For convenience, this method is referred to as DFT-PLS.

D. MAP Estimate

Alternatively, the unknown coefficients of the different DFT basis functions $\{\mathbf{d}_m, m = 0, \ldots, K - 1\}$ can be determined in a collective fashion by making use of the statistics of the image data. For convenience, define $\mathbf{G} \triangleq [\mathbf{g}_1^T, \mathbf{g}_2^T, \ldots, \mathbf{g}_K^T]^T$, which is a vector denoting the collection of acquired (sinogram) data in all K gates; similarly, let $\mathbf{D} \triangleq [\mathbf{d}_0^T, \mathbf{d}_1^T, \ldots, \mathbf{d}_{K-1}^T]^T$, the collection of unknown coefficients of all K harmonic components.

We seek a MAP estimate of the unknown coefficients, i.e.,

$$\widehat{\mathbf{D}} = \arg\max_{\mathbf{D}} [\log p(\mathbf{G};\mathbf{D}) + \log p(\mathbf{D})] \quad (9)$$

where $p(\mathbf{G};\mathbf{D})$is the likelihood function of $\mathbf{G}$ parameterized by $\mathbf{D}$, and $p(\mathbf{D})$ is a prior distribution on $\mathbf{D}$.

The prior term $p(\mathbf{D})$ in (9) is used to enforce spatial smoothness in the reconstructed images, thereby to further reduce the impact of noise. Specifically, we use a Gibbs prior of the form

$$p(\mathbf{D}) \propto \exp\{-\beta_s U_s(\mathbf{D})\} \quad (10)$$

where $U_s(\mathbf{D})$ is an energy term defined in terms of the images as

$$U_s(\mathbf{D}) = \sum_{k=1}^{K} \sum_{j=1}^{N} \sum_{i \in \aleph_j} [f_k(j) - f_k(i)]^2 \quad (11)$$

where $\aleph_j$ denotes a 26-voxel neighborhood around voxel j. In (10), β_s is a scalar weighting parameter used to control the degree of spatial smoothing; it is noted that, for convenience, here the same notation β_s is used as previously in (6) for the weighting parameter, though in principle they may not necessarily assume the same value.

Substituting the representation model in (2) into (11) and applying the Parserval's identity, we can rewrite (11) as

$$U_s(\mathbf{D}) = \sum_{m=0}^{K-1} \sum_{j=1}^{N} \sum_{i \in \aleph_j} |d_m(j) - d_m(i)|^2. \quad (12)$$

From (12), we observe that the energy term in (11) is now expressed directly in terms of the unknown harmonic coefficients. Moreover, it is worth noting from (8) that $U_s(\mathbf{D}) = \sum_{m=0}^{K-1} \|\mathbf{Q}\mathbf{d}_m\|^2$.

In SPECT, the projection data are characterized by Poisson noise. Thus, the log-likelihood function in (9) has the following form:

$$\log p(\mathbf{G};\mathbf{D}) = \sum_{k=1}^{K} \sum_{i=1}^{M} \{-(\mathbf{H}\mathbf{f}_k)(i) - r_k(i) + g_k(i) \log[(\mathbf{H}\mathbf{F}_k)(i) + r_k(i)]\} \quad (13)$$

where $\mathbf{f}_k$ is parameterized by $\mathbf{D}$ as in (2), $(\mathbf{H}\mathbf{f}_k)(i)$ denotes the ith component of $(\mathbf{H}\mathbf{f}_k)$, $r_k(i)$ is the ith component of $\mathbf{r}_k$ and M is the total number of detector bins used.

With all the terms defined, the MAP estimation in (9) can be solved by minimizing the following objective function:

$$\mathbf{J}(\mathbf{D}) = \sum_{k=1}^{K} \sum_{i=1}^{M} \{(\mathbf{H}\mathbf{f}_k)(i) + r_k(i) - g_k(i) \log[(\mathbf{H}\mathbf{f}_k)(i) + r_k(i)]\} + \beta_s \sum_{m=0}^{K-1} \sum_{j=1}^{N} \sum_{i \in \aleph_j} |d_m(j) - d_m(i)|^2. \quad (14)$$

That is

$$\widehat{\mathbf{D}} = \arg\min_{\mathbf{D}} E[\mathbf{J}(\mathbf{D})]. \quad (15)$$

It is noted that, since the images $\mathbf{f}_k$ are linearly parameterized by **D,** the objective function **J**(**D**) in (14) has essentially a similar mathematical form to that of MAP estimation in emission tomography. Indeed, when all the AC components are included in the representation model, i.e., no temporal regulation is used, the objective function **J**(**D**) in (14) simply amounts to independent reconstruction of individual gates by conventional MAP estimation with a spatial prior. Thus, we can employ a similar approach, such as generalized EM [12], for the optimization in (15). As noted earlier, when the activity function in (2) is real-valued, the coefficients $\mathbf{d}_m$ are conjugate symmetric, i.e., $\mathbf{d}_m = \bar{\mathbf{d}}_{K-m}$. In such a case, we can explicitly substitute the coefficients $\mathbf{d}_m$, $m = K/2+1, \ldots, K-1$, by their conjugate symmetric counterparts $\bar{\mathbf{d}}_{K-m}$ in the objective function $J(\mathbf{D})$ in (14); as a consequence, $J(\mathbf{D})$ becomes a function of only $\mathbf{d}_m$, $m = 0,\ldots, K/2$. In our experiments, we applied an iterative coordinate descent (ICD) algorithm [13] in which the unknown coefficients $d_m(j)$ are updated sequentially for each voxel. For completeness, we furnish the details of this algorithm in the Appendix. This algorithm is referred to as DFT-MAP.

III. Evaluation Methods

In our experiments, we evaluated the proposed reconstruction approach in the context of cardiac gated SPECT imaging. We tested both the DFT-PLS and DFT-MAP reconstruction methods described in Section II. To demonstrate the effect of the Fourier representation model, we varied the number of harmonics used, which plays the role of regulating the degree of temporal smoothing across the different gates; in addition, we also varied the spatial parameter β_s to optimize the degree of spatial smoothing. In the following, we describe the details involved in this study, including quantification of reconstruction results and the datasets used.

A. Image Datasets

1) Phantom Data—We first tested the reconstruction algorithms using simulated imaging in a setting that is typical of realistic clinical acquisitions. The use of simulated data allows us to conduct extensive quantitative analyses of the reconstruction results through multiple noise realizations. In our experiments, the 4D NURBS-based cardiac-torso (NCAT) 2.0 phantom [14] was used to generate the source and attenuation distribution, which was derived from real patient anatomy. The SIMIND Monte Carlo package [15] was used to simulate gated SPECT imaging with Tc^{99m} labeled sestamibi as the imaging agent. The SPECT system simulated was the Picker Prism3000 with a low-energy high-resolution (LEHR) collimator. The projections were 64 by 64 bins with a voxel size of 0.634 cm. For a circular camera rotation of 28.5 cm radius, 64 projection sets were collected for each gate frame. A total of 16 gates were used. Two energy windows were used in SIMIND as in [16]: the photo-peak window was 20% (28 keV) centered at 140 keV, and a 3.5 keV window abutted to the lower side of the photopeak window. Poisson noise was introduced at a level of 8 million total counts as in a typical clinical acquisition. The scattered counts were about 34% of the total counts.

As an example, Fig. 1(b) shows an anterior projection of the NCAT phantom in the photopeak window obtained using SI-MIND, where the heart region is notably very noisy.

To estimate the scatter component in the projection data, the filtered TEW method [17], [18] was used. First, an estimate of the scatter counts within the photopeak window was obtained by multiplying the counts in the 3.5 keV window by 4. This estimate was further filtered

with an order-3 2-D Butterworth lowpass filter with a cutoff frequency of 0.2 cycles/cm as suggested in [18]. For attenuation correction, the attenuation map generated by the NCAT program was used.

2) Clinical Data—As a preliminary demonstration, we also tested the reconstruction algorithms on a set of clinical data. This dataset was acquired from a female patient by an IRIX system [19] with 68 projections (3-degree steps) and a 128×128 matrix. The voxel size was 0.467 cm. The acquisition started from right anterior oblique, passed through anterior and left anterior oblique, and ended at left lateral oblique. A total of eight gates were used. The photopeak window was 15% centered at 147.5 keV, and a second 5% window centered at 133.2 keV was used. The total number of counts acquired was 23.8 millions. For attenuation correction, the attenuation map was estimated from the transmission images of the patient.

B. Evaluation Criteria

In cardiac gated SPECT, the main goal is to obtain the image activities concerning the heart. Thus, our evaluation is mainly focused on the accuracy of the reconstructed heart volume. We applied several quantitative criteria, including: 1) the overall accuracy of the reconstructed myocardium measured by signal-to-noise ratio (SNR); 2) bias versus variance analysis for quantifying the regional accuracy of the heart wall; 3) the reconstructed time-activity curve (TAC) of a region of interest (ROI) selected on the heart wall. As explained in the following, the TAC is used to measure the potential effect of temporal smoothing on cardiac motion.

1) Myocardium Reconstruction Accuracy—To quantify the overall accuracy of the reconstructed myocardium, we computed the SNR of a 30 × 28 × 20 volumetric region containing the entire left ventricle (LV), of which a 2-D slice is shown in Fig. 1(a). Specifically, it is defined as

$$\mathrm{SNR}=10\log_{10}\frac{\|\mathbf{F}\|^2}{\|\mathbf{F}-\widehat{\mathbf{F}}\|^2} \quad (16)$$

where $\mathbf{F}=[\mathbf{f}_1^T,\mathbf{f}_2^T,\ldots,\mathbf{f}_K^T]^T$ and $\widehat{\mathbf{F}}=[\widehat{\mathbf{f}}_1^T,\widehat{\mathbf{f}}_2^T,\ldots,\widehat{\mathbf{f}}_K^T]^T$, which denote the reference and reconstructed images, respectively. The SNR defined previously is computed for the myocardium ROI over all the K gates.

2) Regional Bias-Variance Analysis—To quantify the regional accuracy of the reconstructed myocardium, we conducted a bias-variance analysis of an ROI defined on the LV wall [as indicated in Fig. 1(a)]. In cardiac imaging the key interest is to evaluate the tracer distribution of the heart wall, which is used for the diagnosis of the myocardium. The use of “regional bias-variance analysis” is to quantify the accuracy of the reconstructed heart wall [20]. It allows one to decompose the reconstruction error into two terms, namely bias and variance, which are estimated from many different noise realizations. By plotting the variance (or the standard deviation) versus the bias, one can obtain the tradeoff between these two error terms over the operating range of the parameters. Therefore, a bias-variance plot allows one to compare the variance of the different methods at a selected bias, or vice versa.

As explained in the following, this ROI was deliberately selected on the edge of the heart wall in order to quantify any potential smoothing effect on the wall motion by reconstruction

(which would exhibit as a bias in image intensity). Specifically, let $\bar{f}_{\mathrm{ROI}}$ denote the mean intensity of the ROI in the noiseless reference f, i.e.,

$$\bar{f}_{\mathrm{ROI}} = \frac{1}{M} \sum_{i \in \mathrm{ROI}} f(i) \quad (17)$$

where M is the total number of voxels within the ROI. Our goal is to quantify the statistical accuracy of this quantity from different noisy reconstructions.

Let $\hat{f}^{(q)}$, $q = 1, 2, \ldots, Q$ denote the estimates of $\bar{f}_{\mathrm{ROI}}$ obtained from Q different noise realizations. The mean estimate is computed as

$$\hat{\mu} = \frac{1}{Q} \sum_{q=1}^{Q} \bar{\hat{f}}_{\mathrm{ROI}}^{(q)}. \quad (18)$$

Then the bias and standard deviation (std) of this mean estimator are, respectively, estimated as

$$\mathrm{bias} = \frac{|\bar{f}_{\mathrm{ROI}} - \hat{\mu}|}{\bar{f}_{\mathrm{ROI}}} \times 100\%, \text{ and} \quad (19)$$

$$\mathrm{std} = \frac{\sqrt{\frac{1}{Q-1} \sum_{q=1}^{Q} \left(\bar{\hat{f}}_{\mathrm{ROI}}^{(q)} - \hat{\mu} \right)^2}}{\bar{f}_{\mathrm{ROI}}} \times 100\%. \quad (20)$$

In our experiments, a total of $Q = 30$ noise realizations were used.

3) Time Activity Curves (TACs)—To demonstrate the potential effect of temporal smoothing on cardiac motion, we also computed the TAC of the ROI on the LV wall as defined previously [Fig. 1(a)]. As noted previously, this ROI was deliberately selected on the edge of the wall. Thus, as the heart wall moves in and out of this ROI during the cardiac cycle, its image intensity will vary accordingly, which, therefore, serves as a good indicator of the degree of wall motion in the reconstructed images. In our experiments, the image intensity of this ROI was computed and plotted as a function of the different gates.

Finally, as reference for comparison, the gated images were reconstructed from simulated projection data of the phantom under the condition of no noise and without attenuation and scatter (by turning off attenuation and scatter in the simulation) using the ML-OSEM algorithm [21] (10 iterations, 16 subsets). These images were then used as reference for quantifying the accuracy of reconstructed images as described above. Such a choice was based upon the following considerations. In the simulated imaging study, we used a setting that is typical of realistic clinical acquisitions. That is, the projection data were obtained from the SIMIND Monte Carlo package [15] which simulates the generation, propagation, scattering and detection of photons. It is important to note that this is more realistic than simulation with a discretized analytical projector, as it would remove any potential bias that may arise if the same analytical projection model were used for both data generation and reconstruction. In reality, there always exists a modeling error between the actual data acquisition process and the analytical projector used for the reconstruction. Because of this

potential mismatch in the projector model, the noiseless reconstruction represents what would be achievable in the ideal scenario of both perfect attention and scatter correction and perfect noise filtering. By comparing to this noiseless reconstruction, we will learn how far the proposed method is from this ideal situation.

IV. Results and Discussions

A. Overall Reconstruction Accuracy

In Fig. 2, we summarize the SNR results of the reconstructed myocardium by the proposed DFT-PLS and DFT-MAP methods with different parametric settings. In the figure, each curve was obtained by varying the order of Fourier representation (abscissa) while the spatial parameter β_s was held at a constant. The results were shown for several different values of β_s for each method, namely, $[0,1,3] \times 10^{-3}$ for DFT-PLS and $[0,1,2] \times 10^{-4}$ for DFT-MAP. These results were obtained from an average of 30 different noise realizations.

From Fig. 2, we see that both methods achieved nearly the same highest SNR level (approximately 17 dB) with one AC component. For both methods the SNR of the reconstructed myocardium decreases monotonically as the order of the AC components in Fourier representation further increased in the reconstruction. This shows that the noise level becomes increasingly dominant over the signal at higher order AC components. Note that when the model order is eight, the DFT-MAP is equivalent to that of independent reconstruction of individual gates by using MAP with a spatial prior.

The results in Fig. 2 indicate that, as far as the overall noise level in the entire myocardium is concerned, the best SNR results were achieved when the model order is at one. However, this setting may not be optimal as far as the regional wall motion is concerned, as our regional analysis results in the following will indicate. In Fig. 3, we show the power spectrum of the signal in the entire myocardium ROI (computed from the noiseless reference images), which shows that up to 89.87% of the AC signal power can be captured by the first harmonic component. Thus, inclusion of additional higher-order coefficients has little effect on further improving the SNR of the entire ROI. However, the overall SNR measure does not provide an adequate assessment of the accuracy of the heart wall associated with regional wall motion, which is important in diagnostic cardiac imaging. Because of this, we have also used additional measures such as regional bias-variance analysis and time-activity curves which are shown in the following.

In order to speed up the reconstruction, in our experiments we first estimated the extent of the heart volume by a bounding box, and only the DC component was used in the representation model for background voxels outside this bounding box. This is because in a gated sequence there is little motion outside the heart volume among the different gates (hence, little image intensity variations).

B. Regional Bias-Variance Results

In Fig. 4, we show plots of bias versus standard deviation for the ROI on the heart wall [Fig. 1(a)] from reconstruction by the different methods. In the figure, each curve was obtained by varying the spatial smoothness parameter β_s ($[0, 0.5,1,3] \times 10^{-3}$ in DFT-PLS; $[0, 0.5,1,2] \times 10^{-4}$ in DFT-MAP) while the order of Fourier representation was held at a constant in the reconstruction. A total of 30 noise realizations were used; the bias and variance values were computed as in (19) and (20).

From Fig. 4, we see that each curve shows that as β_s increases the variance (ordinate) decreases while the bias (abscissa) increases. Furthermore, increasing the order of the Fourier representation will decrease the bias, but the variance will increase; the smallest bias

is reached once the model order is increased to four. Beyond that there seems to be little additional benefit. On the other hand, the largest bias is achieved when the model order is at one. This increased bias is attributed to the overly smoothing effect of the temporal regulation in this case.

For comparison, we also tested against a clinical spatiotemporal processing method [22]. In this method, the different gates were first reconstructed by using the filtered backprojection (FBP) method, then processed spatially with a Butterworth filter of order 2.4 and cutoff frequency of 0.2 cycles/voxel, and further processed with a temporal filter with impulse response 1/4, 2/4, 1/4. This method is referred to as ST121. As can be seen in Fig. 4, the ST121 method could achieve a smaller variance but with a much larger bias.

C. TAC Results

In Fig. 5, we show the TAC of the ROI on the heart wall [Fig. 1(a)] from reconstruction by the different methods. The order of Fourier representation used was three. These results were obtained from an average of 30 different noise realizations.

For comparison, the TAC obtained with ST121 is also shown in Fig. 5. As can be seen, the TACs of both DFT-PLS and DFT-MAP on average are much closer to that of the reference TAC (hence, smaller bias) than that of ST121. Note that this is consistent with the bias versus variance results shown earlier in Fig. 4. These results indicate that the use of the Fourier representation model did not cause significant blurring of the wall motion in the reconstructed images.

D. Reconstructed Images

In Fig. 6, we show a set of typical images reconstructed by the different methods, namely, DFT-PLS, DFT-MAP, ST121, and the noiseless reference. These images are in fully 3-D. For clarity, only one transverse slice (#36) of the LV myocardium is shown for several selected gates; in addition, in Fig. 7 we show a short-axis view of these reconstructed images.

From these results it can be seen that the DFT-PLS and DFT-MAP images suffer from far less blur than that of ST121; the LV wall in DFT-PLS and DFT-MAP is notably better defined, particularly near the ES phase (gate #9). The images in Fig. 6 show that the septal wall of the LV is also more accurate in DFT-PLS and DFT-MAP.

Finally, in Fig. 8, we show a plot of the objective function versus the number of iterations for DFT-PLS and DFT-MAP in a typical run for the simulated data. For DFT-PLS, the plot is shown for the case of reconstruction of the DC component when spatial parameter $\beta_s = 0$; for DFT-MAP, the plot is shown for the case of reconstruction with model order at one and the spatial parameter $\beta_s = 0$.

E. Clinical Data

As a preliminary demonstration, in Fig. 9, we show the reconstructed images from the set of clinical data by the different methods. Owing to the lack of ground truth, the parameters for DFT-PLS and DFT-MAP were empirically chosen (for DFT-PLS $\beta_s = 5 \times 10^{-4}$; for DFT-MAP $\beta_s = 2 \times 10^{-6}$; the order of Fourier representation was two for both). As can be seen, the LV wall is better defined in DFT-PLS and DFT-MAP, and the heart wall is better resolved from the high bowel activities nearby.

Finally, it is noted that from all the results in this section the two reconstruction methods, DFT-PLS and DFT-MAP, achieved very similar reconstruction results when evaluated with

different criteria. While in theory the DFT-PLS approach is only suboptimal compared to DFT-MAP, the reconstruction results show that it can be nearly as accurate as DFT-MAP. We believe that this is largely because the DFT representation could effectively decouple the statistical dependency among the different harmonics, as a result, reconstructing them jointly may offer little advantage over otherwise. Among the two, the DFT-PLS method is noted to be more efficient computationally.

V. Conclusion

We developed a reconstruction procedure for gated imaging by using Fourier harmonic basis functions. A PLS estimation method and a MAP estimation method were applied for the reconstruction, in which the Fourier representation plays the role of an implicit temporal prior. We demonstrated the proposed approach in the context of gated cardiac SPECT imaging, where the image data are deteriorated by the increased noise due to gating, distance-dependent blur, attenuation and scatter. Our quantitative results show that the proposed approach can yield more accurate reconstruction of the gated images compared to a clinical post-temporal filtering approach. We also demonstrated our approach on a set of real patient data. Interestingly, our proposed DFT-PLS and DFT-MAP methods performed similarly in reconstructing gated heart image sequences. Encouraged by these promising results, we plan to further evaluate this approach on the detection of heart perfusion defect and cardiac motion tracking in future studies.

Acknowledgments

This work was supported by the National Institutes of Health under Grant HL65425. The associate editor coordinating the review of this manuscript and approving it for publication was Dr. Rick P. Millane.

The authors would like to thank Dr. M. A. King from the University of Massachusetts Medical School for providing the clinical dataset used in this study.

References

1. Garcia EG. Imaging guidelines for nuclear cardiology procedures part I. J Nucl Card. 1996; 3:G1–G46.
2. Low DA, Nystrom M, Kalinin E, Parikh P, Dempsey JF, Bradley JD, Mutic S, Wahab SH, Islam T, Christensen G, Politte DG, Whiting BR. A method for the reconstruction of four-dimensional synchronized CT scans acquired during free breathing. Med Phys. 2003; 30(6):1254–1263. [PubMed: 12852551]
3. Lamare F, Carbayo MJL, Cresson T, Kontaxakis G, Santos A, Rest CCL, Reader AJ, Visvikis D. List-mode-based reconstruction for respiratory motion correction in PET using non-rigid body transformations. Phys Med Biol. 2007; 52:5187–5204. [PubMed: 17762080]
4. Osman NF, McVeigh ER, Prince JL. Imaging heart motion using harmonic phase MRI. IEEE Trans Med Imag. Mar; 2000 19(3):186–202.
5. Klein GJ, Reutter BW, Huesman RH. Non-rigid summing of gated PET via optical flow. IEEE Trans Nucl Sci. Aug; 1997 44(4 pt 1):1509–1512.
6. Vanhove C, Franken PR, Defrise M, Deconinck F, Bossuyt A. Reconstruction of gated myocardial perfusion SPET incorporating temporal information during iterative reconstruction. Eur J Nucl Med Molec Imag. 2002; 29(4):465–472.
7. Gravier E, Yang Y, Jin M. Tomographic reconstruction of dynamic cardiac image sequences. IEEE Trans Image Process. Apr; 2007 16(4):932–942. [PubMed: 17405427]
8. Niu, X.; Jin, M.; Yang, Y. Reconstruction of gated cardiac SPECT using DFT basis functions; Proc Asilomar Conf Signals Syst Comput; 2007. p. 756-760.
9. Niu X, Yang Y, Wernick M. 4d reconstruction of cardiac images using temporal fourier basis functions. Proc IEEE Int Conf Image Process. 2008:2944–2947.

10. Kaufman L. Maximum likelihood, least squares, and penalized least squares for PET. IEEE Trans Med Imag. Feb; 1993 12(2):200–214.
11. Qi J, Leahy RM. Iterative reconstruction techniques in emission computed tomography. Phys Med Biol. 2006; 51:R541–R578. [PubMed: 16861768]
12. Herbert T, Leahy R. A generalized EM algorithm for 3-D Bayesian reconstruction from Poisson data using Gibbs priors. IEEE Trans Med Imag. Jun; 1989 8(2):194–202.
13. Bouman CA, Sauer K. A unified approach to statistical tomography using coordinate descent optimization. IEEE Trans Image Process. Mar; 1996 5(3):480–492. [PubMed: 18285133]
14. Segars, WP. PhD dissertation. Univ. North Carolina; Chapel Hill, NC: 2001. Development of a new dynamic NURBS-based cardiactorso (NCAT) phantom.
15. Ljungberg M, Strand SV. A monte carlo program simulating scintillation camera imaging. Comp Meth Prog Biomed. 1989; 29:257–272.
16. Ogawa K, Ichihara T, Kubo A. Accurate scatter correction in single photon emission CT. Ann Nucl Med Sci. 1994; 7:145–150.
17. Ogawa K, Harata Y, Ichihara T, Kubo A, Hashimoto S. A practical method for position-dependent compton-scatter correction in single photon emission CT. IEEE Trans Med Imag. Sep; 1991 10(3): 408–412.
18. King MA, deVries DJ, Pan TS, Pretorius PH, Case JA. An investigation of the filtering of TEW scatter estimates used to compensate for scatter with ordered subset reconstruction. IEEE Trans Nucl Sci. Jun; 1997 44(3 pt 2):1140–1145.
19. Gagnon D, Tung CH, Zeng L, Hawkins WG. Design and early testing of a new medium-energy transmission device for attenuation correction in SPECT and PET. Proc 1998 IEEE Med Imag Conf. 1999:1349–1353.
20. Dey J, King MA. Theoretical and numerical study of MLEM and OSEM reconstruction algorithms for motion correction in emission tomography. IEEE Trans Nucl Sci. Oct; 2009 56(5 pt 1):2739–2749. [PubMed: 20419053]
21. Hudson HM, Larkin RS. Accelerated image reconstruction using ordered subsets of projection data. IEEE Trans Med Imag. Dec; 1994 13(4):601–609.
22. Jin M, Yang Y, Niu X, Marin T, Brankov JG, Feng B, Pretorius PH, King MA, Wernick MN. Quantitative evaluation study of four-dimensional gated cardiac SPECT reconstruction. Phys Med Biol. 2009; 54:1–17. [PubMed: 19060362]
23. Nash, SG.; Sofer, A. Linear and Nonlinear Programming. New York: McGraw-Hill; 1996.

Biographies

Xiaofeng Niu (S’08) received the B.S. degree in electrical engineering from Nankai University, Tianjin, China, in 2003, and the M.S. degree in electrical engineering from the Graduate University of Chinese Academy of Science, Beijing, China, in 2006, and is currently pursuing the Ph.D. degree in electrical engineering at Illinois Institute of Technology, Chicago, IL.

His current research is focused on signal and image processing, medical imaging, and pattern recognition.

Yongyi Yang (M'97–SM'03) received the B.S.E.E. and M.S.E.E. degrees from Northern Jiaotong University, Beijing, China, in 1985 and 1988, respectively, and the M.S. degree in applied mathematics and the Ph.D. degree in electrical engineering from the Illinois Institute of Technology (IIT), Chicago, IL, in 1992 and 1994, respectively.

He is currently on the faculty of the Department of Electrical and Computer Engineering, IIT, where he is a Professor. Prior to this position, he was a faculty member with the Institute of Information Science, Northern Jiaotong University. His research interests are in signal and image processing, medical imaging, machine learning, pattern recognition, and biomedical applications. He is a coauthor of *Vector Space Projections: A Numerical Approach to Signal and Image Processing, Neural Nets, and Optics* (Wiley, 1998).

Dr. Yang is an Associate Editor for the IEEE Transactions on Image Processing.

Appendix Iterative DFT-MAP Algorithm

For the optimization in (15), we applied a generalized EM algorithm [12]. First, as in EM, introduce the complete data as the set of random variables s_{ij}, each being the number of photons emitted from within pixel j and detected in projection bin i. Then the estimate $\mathbf{D}$ of is updated at each iteration as

$$\widehat{\mathbf{D}}^n = \arg\min_{\mathbf{d}} \{E[-\log p(\mathbf{s};\mathbf{D})|\mathbf{G};\widehat{\mathbf{D}}^{n-1}] + \beta_s U_s(\mathbf{D})\} \quad (21)$$

In SPECT, the log-likelihood of the complete data is given by

$$\log p(\mathbf{s};\mathbf{D}) = \sum_{k=1}^{K}\sum_{j=1}^{N}\sum_{i=1}^{M}[s_{ij}\log(h_{ij}f_k(j)) - h_{ij}f_k(j) - \log(s_{ij}!)] \quad (22)$$

where it is understood that the quantity $\mathbf{f}_k$ is parameterized by $\mathbf{D}$ as in (2).

As in EM, define the Q function as

$$Q(\mathbf{D}, \widehat{\mathbf{D}}^{n-1}) = E[\log p(\mathbf{s};\mathbf{D})|\mathbf{G};\widehat{\mathbf{D}}^{n-1})]. \quad (23)$$

By ignoring the term $\log(s_{ij}!)$ which is not related to $\mathbf{D}$, the function Q can be written as

$$Q(\mathbf{D}, \widehat{\mathbf{D}}^{n-1}) = \sum_{k=1}^{K}\sum_{i=1}^{M}\sum_{j=1}^{N}[p_{ij}^k \log(h_{ij}f_k(j)) - h_{ij}f_k(j)] \quad (24)$$

where

$$p_{ij}^{k} \triangleq E[\, s_{ij} | \mathbf{G}; \widehat{\mathbf{D}}^{n-1}] = \frac{h_{ij} \widehat{f_k}(j)}{(\mathbf{H}\widehat{\mathbf{f}_k})\,(i) + r_k(i)} g_k(i). \quad (25)$$

Then the update in (21) can be rewritten as

$$\widehat{\mathbf{D}}^{n} = \arg\min_{\mathbf{d}} \{ -Q(\mathbf{D}, \widehat{\mathbf{D}}^{n-1}) + \beta_s U_s(\mathbf{D}) \}. \quad (26)$$

In our experiments, we implemented an iterative coordinate descent (ICD) algorithm [13] for computing the update in (26), in which the unknown coefficients $d_m(j)$ are updated sequentially for each voxel. Specifically, consider voxel j. Let vector $\mathbf{d}$ denote the collection of unknown coefficients associated with j, i.e., $\mathbf{d} \triangleq [d_0(j), d_1(j), \ldots, d_{K-1}(j)]^T$, and let $h(\mathbf{d})$ denote the objective function in (26) restricted to only $\mathbf{d}$, with the rest of the voxels fixed at their current estimate. The unknown $\mathbf{d}$ is then solved from minimization of $h(\mathbf{d})$. To ensure that the resulting image intensity is nonnegative, we applied the barrier method [23] for the minimization of $h(\mathbf{d})$. Specifically

$$\mathbf{d} = \arg\min_{\mathbf{d}} \left[h(\mathbf{d}) + \mu \sum_{k=1}^{K} \frac{1}{f_k(j)} \right] \quad (27)$$

where the second term is the barrier function of which the role is to keep the solution from leaving the feasible region. Again, note that in (27) $f_k(j)$ is parameterized by $\mathbf{d}$. In our experiments, the Newton's method was used for solving (27). As starting point, the DC component was set as a uniform (positive) constant as in standard EM reconstruction, and the AC components were set to zero. Such a choice was to insure that the initial iterate resides in the feasible region. The barrier parameter was set to be $\mu = 5/(n + 1)$ with n representing the iteration number.

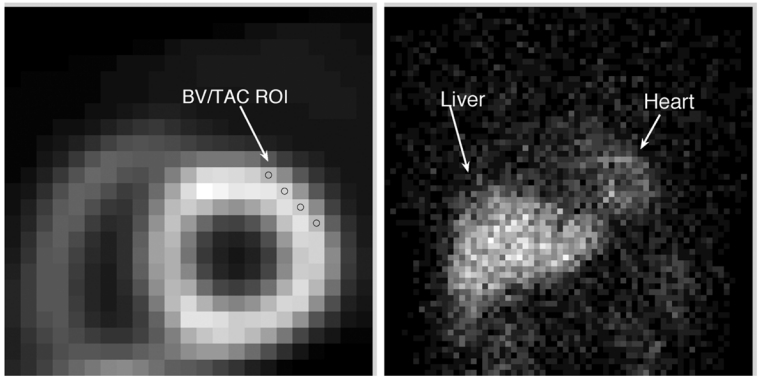

(a) (b)

Fig. 1.
(a) Region of interest (ROI) used for bias-variance (BV) analysis and TAC. (b) Interior projection of NCAT obtained using SIMIND.

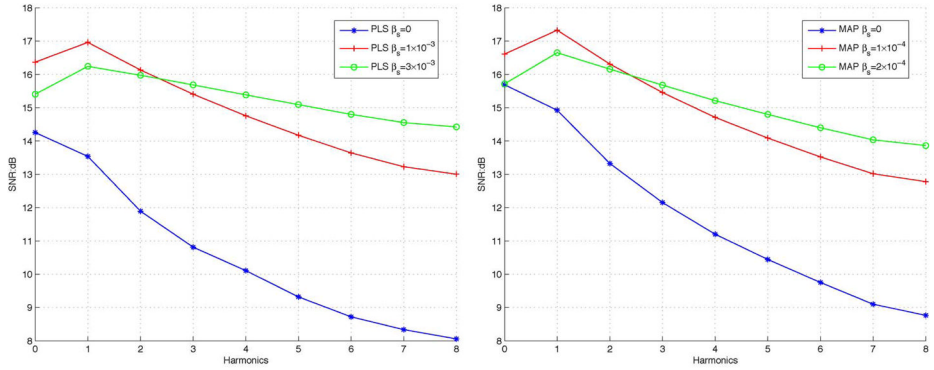

(a) (b)

Fig. 2.

Signal-to-noise ratio (SNR) of the reconstructed LV myocardium with different settings of β_s and different numbers of harmonics for DFT-PLS and DFT-MAP. These results were obtained from 30 noise realizations.

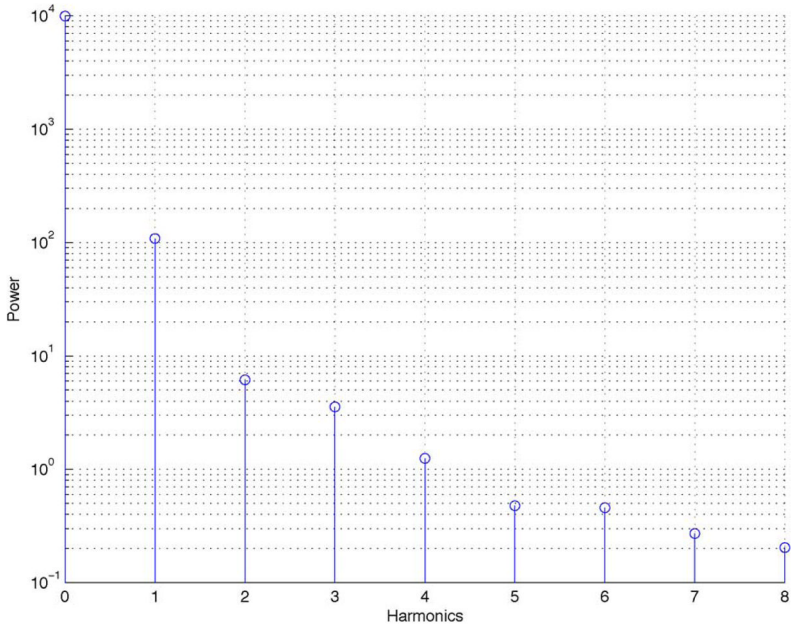

Fig. 3.
Power spectrum of the signal in the myocardium ROI.

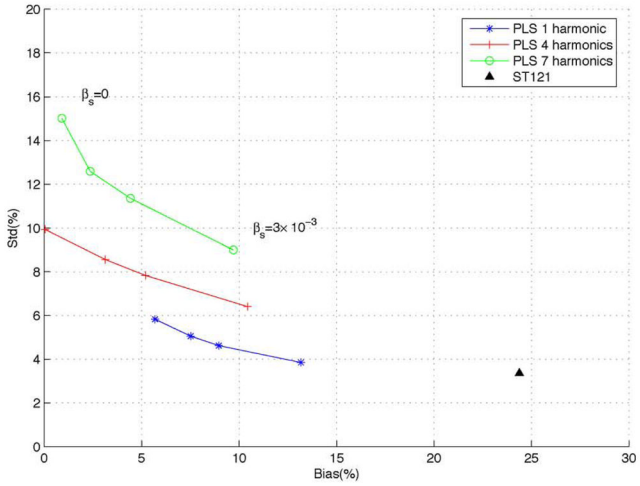

(a)

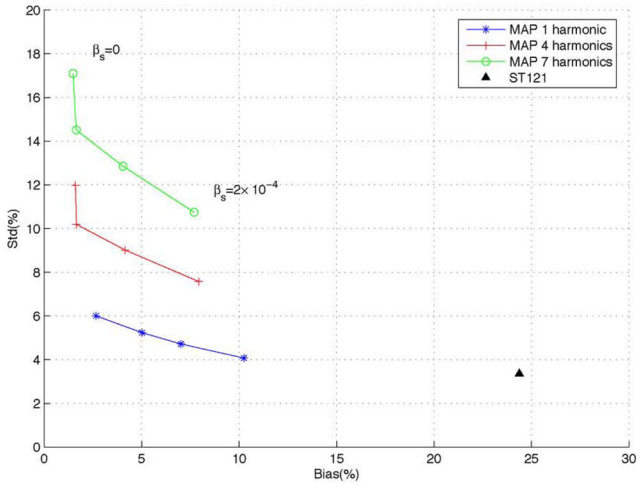

(b)

Fig. 4.

Bias-standard deviation plots for DFT-PLS and DFT-MAP with different settings of β_s and numbers of harmonics. These results were obtained from 30 noise realizations. For reference the result is also shown for ST121.

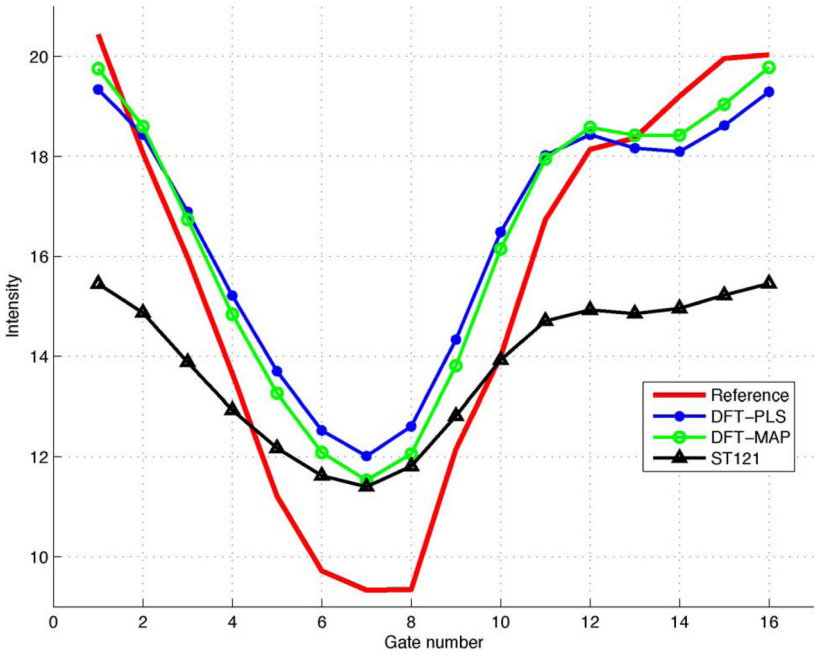

Fig. 5.

Mean time activity curves across 16 gates obtained with different methods: DFT-PLS, DFT-MAP, and ST121. A total of 30 noise realizations were used.

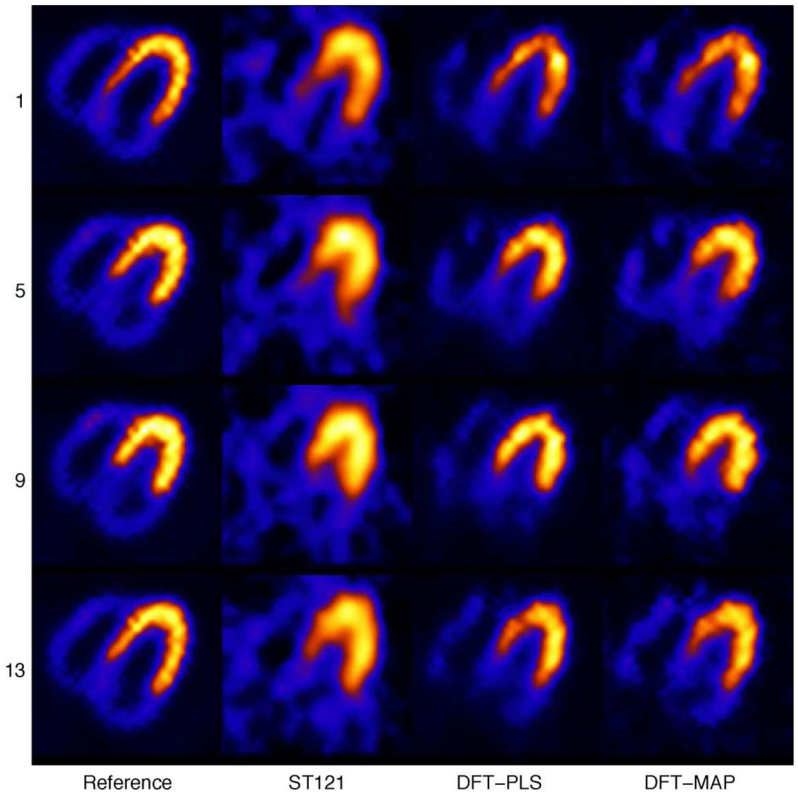

Fig. 6.
Reconstructed images of a transverse slice of four gates by different reconstruction methods: ST121, DFT-PLS ($\beta_s = 5 \times 10^{-4}$), and DFT-MAP ($\beta_s = 1 \times 10^{-4}$).

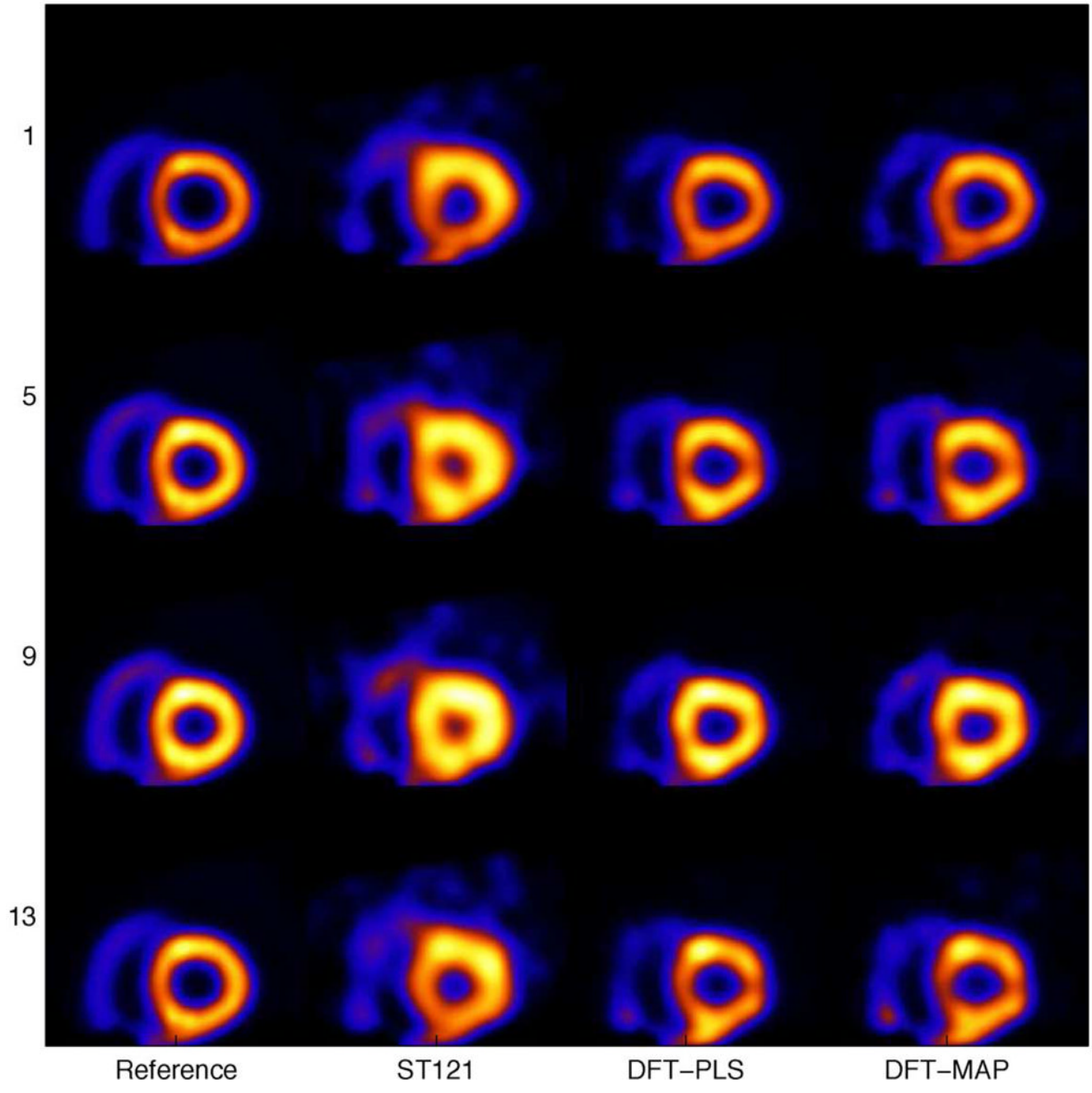

Fig. 7.

Reconstructed images of four gates by different reconstruction methods in short-axis view: ST121, DFT-PLS ($\beta_s = 5 \times 10^{-4}$), and DFT-MAP ($\beta_s = 1 \times 10^{-4}$).

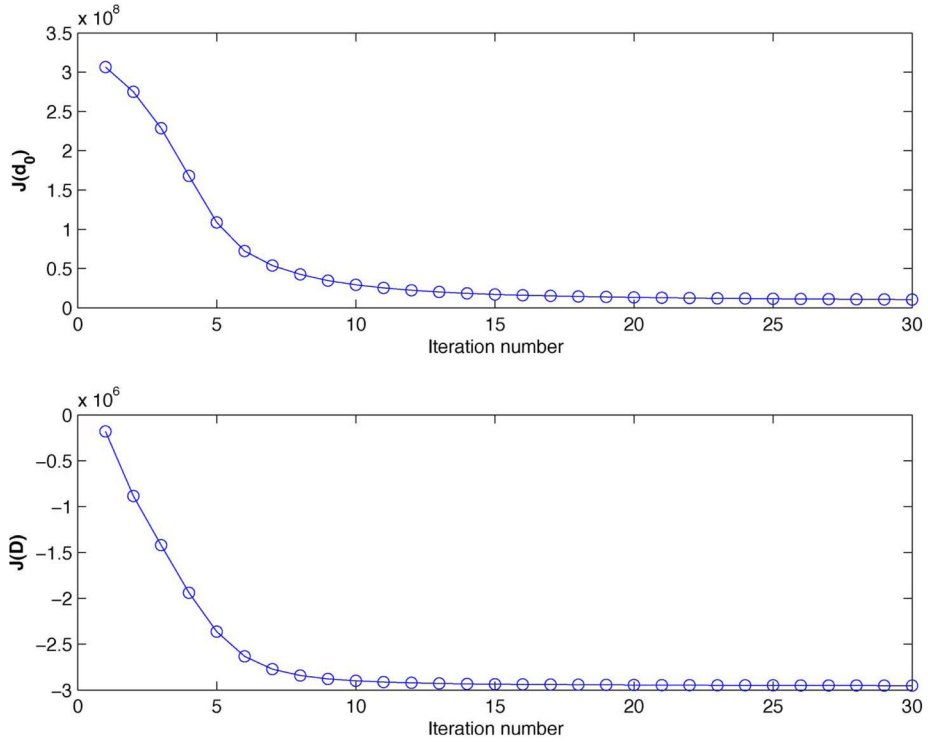

Fig. 8.
Objective function values versus the number of iteration for DFT-PLS and DFT-MAP.

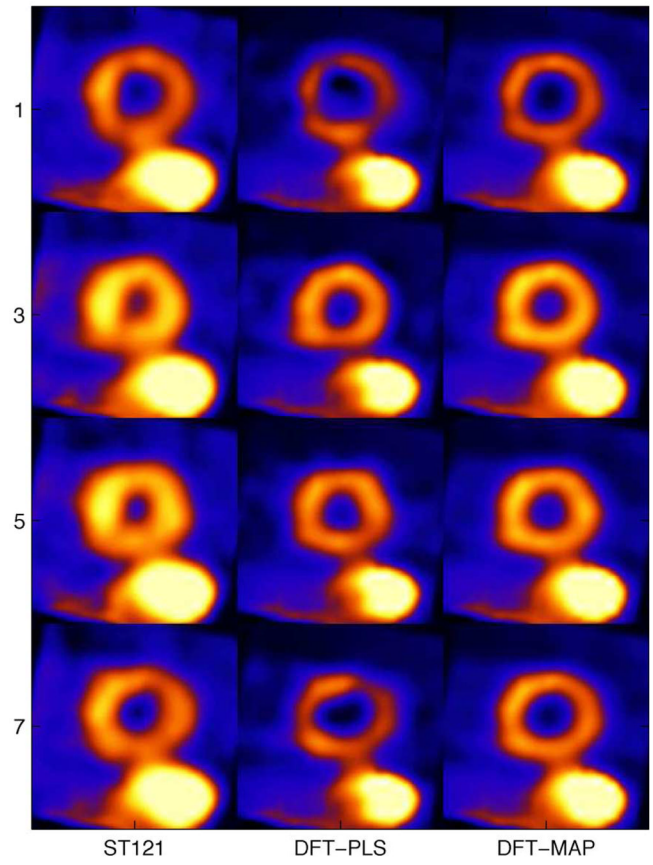

Fig. 9.
Reconstructed images of four gates from a set of patient data with ST121, DFT-PLS ($\beta_s = 5 \times 10^{-4}$), and DFT-MAP ($\beta_s = 2 \times 10^{-6}$).